



HAL
open science

SDSS J002531.46-104022.2 at $z = 0.30$: a candidate for the (ultra)luminous infrared galaxy to optical quasar transition

M. Villar-Martín, B. Emonts, M. Rodríguez, M. Pérez Torres, G. Drouart

► To cite this version:

M. Villar-Martín, B. Emonts, M. Rodríguez, M. Pérez Torres, G. Drouart. SDSS J002531.46-104022.2 at $z = 0.30$: a candidate for the (ultra)luminous infrared galaxy to optical quasar transition. Monthly Notices of the Royal Astronomical Society, 2013, 432, pp.2104-2111. 10.1093/mnras/stt538 . hal-03645523

HAL Id: hal-03645523

<https://hal.science/hal-03645523>

Submitted on 11 Aug 2022

HAL is a multi-disciplinary open access archive for the deposit and dissemination of scientific research documents, whether they are published or not. The documents may come from teaching and research institutions in France or abroad, or from public or private research centers.

L'archive ouverte pluridisciplinaire **HAL**, est destinée au dépôt et à la diffusion de documents scientifiques de niveau recherche, publiés ou non, émanant des établissements d'enseignement et de recherche français ou étrangers, des laboratoires publics ou privés.

SDSS J002531.46–104022.2 at $z = 0.30$: a candidate for the (ultra)luminous infrared galaxy to optical quasar transition[★]

M. Villar-Martín,^{1†} B. Emonts,^{1,2} M. Rodríguez,³ M. Pérez Torres³ and G. Drouart^{4,5}

¹Centro de Astrobiología (INTA-CSIC), Carretera de Ajalvir, km 4, E-28850 Torrejón de Ardoz, Madrid, Spain

²CSIRO Astronomy and Space Science, Australia Telescope National Facility, PO Box 76, Epping NSW 1710, Australia

³Instituto de Astrofísica de Andalucía (CSIC), Glorieta de la Astronomía s/n, E-18008 Granada, Spain

⁴European Southern Observatory (ESO), Karl Schwarzschild Str. 2, D-85748, Garching bei München, Germany

⁵Institut d'Astrophysique de Paris (IAP), 98B Boulevard Arago, F-75014 Paris, France

Accepted 2013 March 25. Received 2013 March 15; in original form 2012 November 15

ABSTRACT

Using data obtained with the Australia Telescope Compact Array (ATCA), we have characterized the amount, spatial distribution and kinematics of the molecular gas in the merging, double-nucleus type 2 quasar (QSO) SDSS J002531.46–104022.2 (hereafter SDSS J0025–10) at $z = 0.30$ using the CO(1–0) transition. This is one of the scarce examples of quasar host galaxies where the CO emission has been resolved spatially at any redshift. We infer a molecular gas mass $M_{\text{H}_2} = (6 \pm 1) \times 10^9 M_{\odot}$, which is distributed in two main reservoirs separated by ~ 9 kpc. It has been found that ~ 60 per cent of the gas is in the central region, associated with the QSO nucleus and/or the intermediate region between the two nuclei. The other 40 per cent is associated with the northern tidal tail and is therefore unsettled. With its high infrared (IR) luminosity $L_{\text{IR}} = (1.1 \pm 0.3) \times 10^{12} L_{\odot}$, SDSS J0025–10 is an analogue of local luminous infrared galaxies (LIRGs with high $L_{\text{IR}} > \text{several} \times 10^{11} L_{\odot}$) and ultraluminous infrared galaxies (ULIRGs). The clear evidence for an ongoing major merger of two gas-rich progenitors, the high L_{IR} dominated by a starburst, the massive reservoir of molecular gas, with a large fraction still unsettled, and the quasar activity are all properties consistent with a transition phase in the (U)LIRG–optical QSO evolutionary scenario. We propose that we are observing the system during a particular transient phase, prior to more advanced mergers where the nuclei have already coalesced. We argue that a fraction of the molecular gas reservoir is associated with a tidal dwarf galaxy identified in the optical *Hubble Space Telescope* image at the tip of the northern tidal tail. The formation of such structures is predicted by simulations of colliding galaxies.

Key words: galaxies: evolution – galaxies: interactions – quasars: individual: SDSS J002531.46–104022.2.

1 INTRODUCTION

CO studies of type 1 quasars (QSO1s) at different redshifts have provided accumulating evidence that QSO1s often contain an abundant supply of molecular gas. At redshift $z < 0.5$, the range of molecular gas masses spans at least two orders of magnitude. Some quasars have $M_{\text{H}_2} \lesssim 10^8 M_{\odot}$, which is significantly lower than the Milky Way (a few $\times 10^9 M_{\odot}$), and others contain giant reservoirs $> 10^{10} M_{\odot}$. At high redshift ($z > 2$), quasars contain $M_{\text{H}_2} \sim \text{several} \times 10^9$ to $\sim 10^{11} M_{\odot}$ (e.g. Bertram et al. 2007; Xia et al.

2012). As has been found for other galaxy types, Bertram et al. (2007) and Xia et al. (2012) have shown that quasars with the highest infrared (IR) luminosities also contain the largest M_{H_2} .

In recent years, there has been quite an active investigation of the molecular gas content of type 2 quasars (QSO2s),¹ although this has almost invariably focused on high-redshift (i.e. $z > 2$) objects (e.g. Martínez Sansigre et al. 2009) and with scarce spatial information.

Regarding studies of the molecular gas content of quasars in general, the intermediate redshift range ($0.1 \lesssim z \lesssim 1.5$) has remained

[★]Based on observations carried out with the Australia Telescope Compact Array.

[†]E-mail: villarmm@cab.inta-csic.es

¹We refer to QSO2s as radio-quiet objects, in contrast to narrow-line radio galaxies.

practically unexplored until very recently (Xia et al. 2012; Krips, Neri & Cox 2012; Villar-Martín et al. 2013). This redshift range spans ~ 60 per cent of the age of the Universe, an epoch of declining cosmic star formation rate (Hopkins & Beacom 2006). The results for QSO2s at redshift $z < 0.5$ have been published only in the last year (Krips et al. 2012; Villar-Martín et al. 2013). These suggest that QSO2s often harbour large reservoirs of molecular gas ($\sim \text{several} \times 10^9 M_{\odot}$), similar to QSO1s of similar IR luminosity.

Detailed studies of the spatial distribution of the molecular gas in quasar host galaxies are of special interest. This gas is highly sensitive to the different mechanisms at work during galactic evolution. As such, it retains relic information about the global history of the systems. The spatial redistribution of the molecular gas during the interactions/merger processes is determinant on the triggering of the starburst and (probably) the quasar activities (Bessiere et al. 2012; Ramos Almeida et al. 2012). However, powerful negative feedback might be able to counteract this by cleaning and/or destroying the molecular gas reservoirs, and so quenching the star formation and quasar activities (Hopkins & Beacom 2006).

Such studies have been very scarce and have also mostly focused on the highest redshift QSO1s (e.g. Carilli et al. 2002). So far, the main reasons for this have been the lack in sensitivity and the narrow bandwidths of (sub)millimetre telescopes, as well as the fact that major interest has been directed towards the most distant sources. Spatially resolved data on QSOs in the local and intermediate redshift ($z < 1.5$) Universe are also limited in number (e.g. Staguhn et al. 2004; Krips et al. 2007; Papadopoulos et al. 2008; Feruglio et al. 2010; Aravena et al. 2011). So far, the results have indicated that a large fraction of the molecular gas in low- z quasars – as well as in luminous ($10^{11} \leq L_{\text{IR}}/L_{\odot} < 10^{12}$) and ultraluminous ($10^{12} \leq L_{\text{IR}}/L_{\odot} < 10^{13}$) infrared galaxies (LIRGs and ULIRGs) – is highly concentrated in the galactic centres, most frequently in rotating discs and rings of \lesssim a few kpc in diameter (e.g. Bryant & Scoville 1999; Westmoquette et al. 2012). At intermediate z , some systems have extended and massive reservoirs of molecular gas, associated with companion objects and/or tidal structures (Papadopoulos et al. 2008; Aravena et al. 2011).

In this paper, we present a detailed study of the spatial distribution of the molecular gas traced by the CO(1–0) transition in SDSS J002531.46–104022.2 (hereafter SDSS J0025–10), a QSO2 at $z = 0.303$ selected from the Sloan Digital Sky Survey (SDSS) database. The CO(1–0) ($\nu_{\text{rest}} = 115.27$ GHz) transition is the transition that is least dependent on the excitation conditions of the gas. This is crucial for deriving reliable estimates of the total molecular gas content, including the widespread, low-density gas that might be subthermally excited (e.g. Papadopoulos et al. 2001; Carilli et al. 2010).

SDSS J0025–10 is of special interest because it is undergoing a strong transformation via a major merger event and it allows us to investigate the distribution and dynamics of the molecular gas during this process. Moreover, it shows evidence of phenomena, frequently found in quasars, that can have a profound impact on the evolution of their hosts (i.e. mergers/interactions, star formation and nuclear outflows). A complete study of this system requires the quantification of the molecular gas content, its spatial distribution and kinematics. This is the purpose of this paper.

1.1 SDSS J0025–10

Villar-Martín et al. (2011a,b, hereafter VM11a and VM11b) have presented a detailed study of this system, based on deep optical imaging and spectroscopic data obtained with the focal

reducer and low-dispersion spectrograph 2 (FORs2) of the Very Large Telescope (VLT). Based on the high [O III] λ 5007 luminosity [$\log(L_{[\text{O III}]}/L_{\odot}) = 8.73$] and other criteria related to the optical emission-line ratios and widths, the object was classified as a QSO2 by Zakamska et al. (2003). This QSO2 is a member of an interacting system. It has two nuclei located at ~ 5 kpc in projection. The velocity shift $\Delta V = -20 \pm 20 \text{ km s}^{-1}$ between them, implied by the optical spectrum (VM11a), is consistent with their relative motion being approximately constrained on the plane of the sky. Thus, the apparent separation is similar to the true separation. One nucleus hosts the quasar and the other is forming stars actively. Tidal tails stretch to the north and south. Their predominance in the broad-band optical images shows that they are dominated by stellar continuum emission, although line emission from ionized gas is also detected.

The optical emission-line spectra reveal extended recent star formation in the companion nucleus (which we sometimes refer to as nuc2) and the northern tidal tail. Because it is only stars with masses of $> 10 M_{\odot}$ and lifetimes of < 20 Myr that contribute significantly to the integrated ionizing flux, this sets an upper limit on the age of the most recent burst of star formation at these locations. Moreover, the compact knots that are visible in the tidal tail – see the *Hubble Space Telescope* (HST) image in Villar-Martín et al. (2012) – are reminiscent of star clusters and/or tidal dwarf galaxies (TDGs). The presence of a young stellar population (< 40 Myr) in the quasar nucleus is also confirmed by fits of the spectral energy distribution (SED) of the optical continuum (Bessiere et al., in preparation).

The quasar nucleus hosts an ionized outflow of uncertain origin – induced by the active galactic nucleus (AGN) and/or starburst – which produces very broad emission-line components with FWHM $\sim 1300 \text{ km s}^{-1}$, and blueshifted by $\sim 80 \text{ km s}^{-1}$ relative to the systemic redshift of the galaxy (VM11b).

We assume $\Omega_{\Lambda} = 0.7$, $\Omega_{\text{M}} = 0.3$ and $H_0 = 71 \text{ km s}^{-1} \text{ Mpc}^{-1}$. At $z = 0.303$, 1 arcsec corresponds to 4.45 kpc.

2 ATCA OBSERVATIONS AND HST ARCHIVE DATA

The observations were performed during 2012 August 2–7 with the Australia Telescope Compact Array (ATCA), a radio interferometer in Narrabri, Australia. The ATCA was configured in the most compact hybrid H75 array configuration. Two 2-GHz bands with 1-MHz channel resolution were centred on the redshifted frequency of the CO(1–0) line (88.439 GHz), providing redundancy in case of technical issues with one of the bands. This resulted in a velocity coverage of 7000 km s^{-1} , a maximum resolution of 3.5 km s^{-1} and a primary telescope beam (i.e. effective field of view) of 32 arcsec. Observations were carried out above an elevation of 35° and under good weather conditions, with system temperatures ranging between 450 and 800 K (depending on the antenna and the elevation of the source) and typical atmospheric seeing fluctuations of $< 150 \mu\text{m}$ (with a phase decorrelation of < 10 per cent; see Middelberg, Sault & Kesteven 2006). The total on-source integration time was 17 h.

The phases and bandpass were calibrated every 7.5 min with a short (~ 2 min) scan on the nearby bright calibrator PKS 0003–066 ($S_{88.4 \text{ GHz}} = 1.8 \text{ Jy}$ at 88.4 GHz), located at a distance of $6^{\circ}.4$ from our target source. Atmospheric amplitude variations were calibrated every 30 min using a paddle scan, and the telescope pointing was updated every hour, or every time the telescope moved $> 20^{\circ}$ on the sky. For absolute flux calibration, Uranus was observed close to our target source.

The off-line data reduction was carried out with the *MIRIAD* software (Sault, Teuben & Wright 1995). We discarded bad data (including data with internal interference or shadowing of an antenna, or data taken during weather conditions that introduced significant phase decorrelation). PKS 0003–066 was used for both phase-dependent as well as time-dependent bandpass calibration, by interpolating the calibration solution obtained every 7.5 min (see Emonts et al. 2011 for details on time-dependent bandpass calibration within *MIRIAD*). Atmospheric opacity variations were corrected by weighting the data according to their ‘above atmosphere’ (i.e. paddle-corrected) system temperature. Flux calibration was applied using *Uranus* (ATCA *Uranus* model version 2012 August), resulting in an absolute flux calibration accuracy of 20 per cent. After Fourier transformation, we obtained a data cube with a robust weighting of +1 (Briggs 1995). The data presented in this paper were binned by 10 channels and subsequently Hanning smoothed to a velocity resolution of 68 km s^{-1} , yielding a noise level of $0.7 \text{ mJy beam}^{-1} \text{ chan}^{-1}$. The synthesized beam size of the data is $6.30 \times 4.39 \text{ arcsec}^2$ (position angle $-85^\circ.3$). Total intensity images were created by summing all of the signal (i.e. without setting a noise threshold) across the velocity ranges in which CO(1–0) was detected. The calculated CO luminosities in this paper have been derived from these total intensity images (see Section 3.1).

No 88.4-GHz radio continuum was detected in the data down to a 5σ limit of 0.5 mJy .

The image from the Wide Field Channel (WFC) of the Advanced Camera for Surveys (ACS) onboard the *HST* was retrieved from the Hubble Legacy Archive (HLA; programme identification 10880 and principal investigator H. Scmitt). The only processing applied was cosmic ray removal. The accuracy of the *HST* astrometry is $\sim 0.3 \text{ arcsec}$ in both coordinates. The accuracy of the CO astrometry is expected to be significantly smaller ($\lesssim 0.1 \text{ arcsec}$; e.g. Papadopoulos et al. 2008).

3 RESULTS

3.1 SDSS J0025–10 is a (U)LIRG

We have constrained the IR luminosity, L_{IR} (inferred from the 8–1000 μm wavelength range) by fitting the source SED defined by the Wide-Field Infrared Explorer (WISE; 3.3, 4.6, 11.6 and 22.1 μm) and *Infrared Astronomical Satellite* (*IRAS*; 60 and 100 μm) photometric measurements, as well as the upper limit on the $\sim 3 \text{ mm}$ continuum measured with the ATCA data (see Fig. 1). Optical photometry has not been used, because this band is known to be a complex mixture of stellar and AGN-related components (scattered and/or direct AGN light and nebular continuum; e.g. Vernet et al. 2001; Tadhunter et al. 2011). To build the SED, we have used the *Spitzer* Wide-area Infrared Extragalactic (SWIRE) template library (Polletta et al. 2008), which contains 25 templates including ellipticals, spirals, starbursts, type 2 and type 1 AGNs and composite starburst + AGN.

The best fit corresponds to the starburst template IRAS 20551–4250 (Fig. 1, dashed line). We infer $L_{\text{IR}} = (1.4 \pm 0.4) \times 10^{12} L_{\odot}$ for this SED. The starburst template NGC 6240, which also produces a reasonable fit, is also shown for illustration (Fig. 1, dot-dashed line) because this LIRG system is similar in many aspects to SDSS J0025–10 (i.e. double nuclei, interacting local LIRG; Tacconi et al. 1999; Tecza et al. 2000). For this SED, $L_{\text{IR}} = (8.2 \pm 0.2) \times 10^{11} L_{\odot}$.

With these two SEDs, we constrain the IR luminosity $L_{\text{IR}} = (1.1 \pm 0.3) \times 10^{12} L_{\odot}$. Taking the uncertainties into account, SDSS

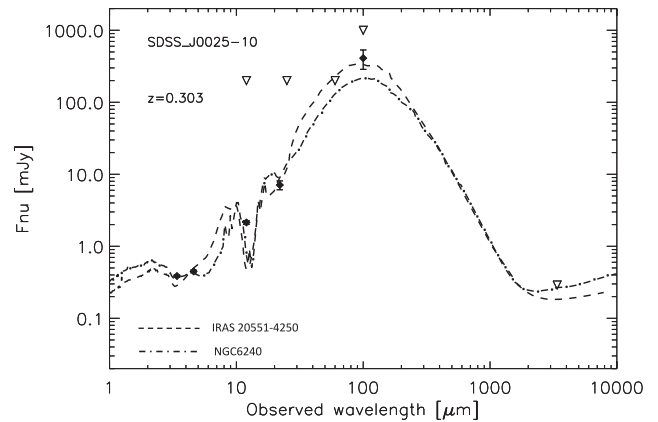


Figure 1. Fit of the NIR to FIR SED of SDSS J0025–10 based on WISE and *IRAS* photometry and the ATCA 3-mm continuum upper limit. Detections and upper limits are marked with diamonds and triangles, respectively. Different line styles are used for the two SEDs, as discussed in the text.

J0025–10 is in the transition range of L_{IR} values between the LIRG and ULIRG regimes.

The fits show that the IR luminosity of SDSS J0025–10 is dominated by a starburst. We calculate the star formation rate as $\text{SFR} = 1.73 \times 10^{-10} \times L_{\text{IR}} (M_{\odot} \text{ yr}^{-1}) = 190 \pm 52 M_{\odot} \text{ yr}^{-1}$, assuming solar abundances and a Salpeter initial mass function (IMF; Kennicutt 1998).

3.2 Mass and spatial distribution of the molecular gas

We measure a total CO(1–0) luminosity in SDSS J0025–10 of $L'_{\text{CO}} = (7.5 \pm 1.5) \times 10^9 \text{ K km s}^{-1} \text{ pc}^2$. Here, L'_{CO} is calculated as

$$L'_{\text{CO}} = 3.25 \times 10^7 \left(\frac{S_{\text{CO}} \Delta V}{\text{Jy km s}^{-1}} \right) \left(\frac{D_L}{\text{Mpc}} \right)^2 \times \left(\frac{v_{\text{rest}}}{\text{GHz}} \right)^{-2} (1+z)^{-1},$$

where $I_{\text{CO}} = S_{\text{CO}} \Delta V$ is the integrated CO(1–0) line intensity in Jy km s^{-1} , D_L is the luminosity distance in Mpc and $v_{\text{rest}} = 115.27 \text{ GHz}$ is the rest-frame frequency of the CO(1–0) transition (Solomon & Vanden Bout 2005). With this L'_{CO} , the system follows the L'_{CO} versus L_{IR} (or L_{FIR}) correlation defined by different types of galaxies (Solomon & Vanden Bout 2005), including QSOs and QSO2s (Bertram et al. 2007; Krips et al. 2012; Villar-Martín et al. 2013). The molecular gas mass is then calculated as $M_{\text{H}_2} = \alpha \times L'_{\text{CO}} = (6 \pm 1) \times 10^9 M_{\odot}$, assuming $\alpha = 0.8 L_{\odot} (\text{K km s}^{-1} \text{ pc}^2)^{-1}$. This value of α is often used in studies of (U)LIRGs and active galaxies (e.g. Downes & Solomon 1998), although a range $\alpha \sim 0.3\text{--}1.3$ is possible (e.g. Sanders & Mirabel 1996; Solomon & Vanden Bout 2005). Similar amounts of molecular gas have been measured for quasars (both type 1 and type 2) of similar IR luminosity and redshift (e.g. Krips et al. 2012; Villar-Martín et al. 2013).

The CO(1–0) line shows a double-horned profile (Fig. 2) with two kinematic components. The blue component has $z = 0.3031 \pm 0.0001$ (which we assume to be the systemic redshift z_{sys}) and $\text{FWHM} = 140 \pm 25 \text{ km s}^{-1}$. The red, fainter component is shifted by $+160 \pm 10 \text{ km s}^{-1}$ and has $\text{FWHM} = 80 \pm 40 \text{ km s}^{-1}$. A negative depression (around $v = 500 \text{ km s}^{-1}$) is also visible in Fig. 2. This feature appears at -2.8σ (when integrated over its full extent). Fig. 2 (bottom) shows that it might be merely a prominent noise peak in

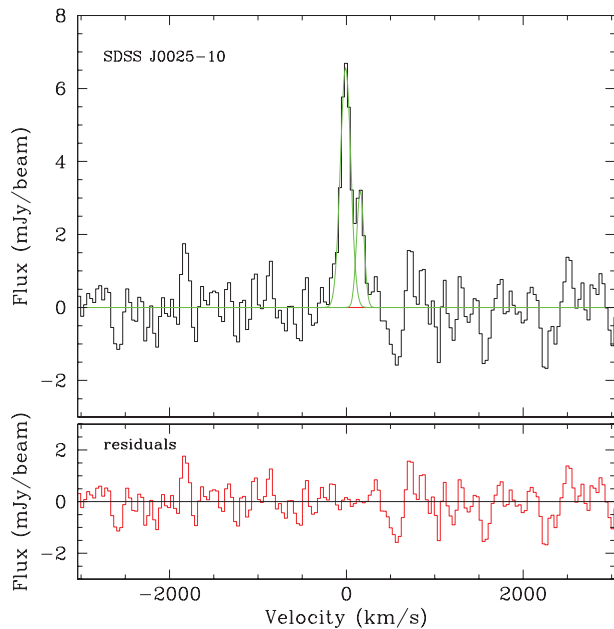


Figure 2. One-dimensional spectrum of SDSS J0025–10, extracted against the QSO2 nucleus (2.3×2.3 arcsec 2). Note the double-horned profile, with Gaussian fits visualizing the two components described in the text. The bottom plot shows the residuals after subtracting the two Gaussian profiles from the spectrum. Velocity values are relative to the peak of the blue component, which we assume to be the systemic velocity ($z = 0.3031 \pm 0.0001$; see text).

the data. Because this negative depression is not noticeably caused by external effects (e.g. weather or phase calibration), it could also indicate that there are low-level systematics affecting the ATCA 3-mm band – similar to the low-level systematics described by Emonts et al. (2011), which occur at the extreme edge of the ATCA 7-mm band, or the possible baseline artefacts mentioned by Norris et al. (2013) in the early wide-band 3-mm ATCA data. Regardless, the integrated blue and red parts of the double-horned CO profile are detected at the 10σ and 7σ significance levels, respectively, and thus unambiguously stand out above the noise, indicating the reliability of the CO emission discussed in this paper.

The spatial distribution of CO(1–0) in different channel maps is shown in Fig. 3 overlaid on the *HST* optical image. The CO(1–0) emission detected at a level $\geq 3\sigma$ spans a range of velocities $\sim [-110, +230]$ km s $^{-1}$, relative to z_{sys} . The CO(1–0) is spatially extended and accumulated in two main reservoirs separated by ~ 2 arcsec or ~ 9 kpc (blue and red contours in Fig. 3, first panel), which we call J0025A and J0025B. The similarity between them, within the errors of the velocity shift, compared to the two kinematic components isolated on the one-dimensional spectrum, suggests that J0025A and J0025B are responsible for the double-horned profile discussed above. J0025A and J0025B have CO luminosities of $(4.3 \pm 0.9) \times 10^9$ and $(3.1 \pm 0.9) \times 10^9$ K km s $^{-1}$ pc 2 , respectively.²

² These values have been derived from the total intensity image in Fig. 3, but have been corrected for line contamination and missed low-level flux based on the Gaussian fitting of the profiles (Fig. 2). This has not significantly changed the values for the blue component, but it has increased both the estimated value and the associated uncertainty of the flux of the red component by 10 per cent. The errors also reflect the 20 per cent uncertainty in absolute flux calibration (see Section 2).

These correspond to $M_{\text{H}_2} = (3.4 \pm 0.7) \times 10^9$ and $(2.5 \pm 0.7) \times 10^9 M_{\odot}$.

In Fig. 4, we show the location of the peaks of the CO(1–0) emission in J0025A and J0025B overlaid on the *HST* image. These locations have been derived by fitting a Gaussian profile to the integrated CO(1–0) emission. Within the uncertainty, this Gaussian profile could be represented by a point source with the size of the synthesized beam. The locations of the CO(1–0) peaks in the different channel maps of Fig. 3 are also plotted, including the uncertainty as a result of the fitting and astrometric errors (see caption for details). From Fig. 4 it is clear that the CO(1–0) emission in J0025B is associated with the northern tidal tail, while J0025A is preferentially associated with the QSO2 nucleus and/or the region between both nuclei.

We do not detect any CO(1–0) emission associated with the companion nucleus, nuc2. However, the star-forming activity it harbours (see Section 1.1) requires a local supply of molecular gas. The H β luminosity from nuc2 (VM11a) implies a line-reddening corrected SFR $\sim 8 M_{\odot} \text{ yr}^{-1}$, assuming $\text{SFR}(M_{\odot} \text{ yr}^{-1}) = 2.3 \times 10^{-41} (L_{\text{H}\beta}/\text{erg s}^{-1})$ for solar abundances and a Salpeter IMF (Kennicutt 1998).³ In turn, this implies $L_{\text{IR}, \text{nuc}2} \sim 4.6 \times 10^{10} L_{\odot}$, which would be a lower limit if part of the star formation were totally obscured (Rodríguez Zaurín et al. 2011). This is ~ 8 per cent of the total L_{IR} of the system. If nuc2 follows the L_{IR} versus L'_{CO} correlation defined by star-forming galaxies (see fig. 8 of Solomon & Vanden Bout 2005), this roughly implies that it contains $\gtrsim 8$ per cent of the total molecular gas or $\gtrsim 5 \times 10^8 M_{\odot}$. The 3σ upper limit for a CO(1–0) non-detection with FWHM = 140 km s $^{-1}$ in our data is $L'_{\text{CO}} = 1.0 \times 10^9$ K km s $^{-1}$ pc 2 , or $M_{\text{H}_2} = 8 \times 10^8 M_{\odot}$. Although the calculations are highly uncertain because of the large scatter of the L_{IR} versus L'_{CO} correlation and because of the uncertainty on the amount of obscured star formation in nuc2, they imply that the CO(1–0) emission likely falls below the detection limit of our data (otherwise, a low-level signal would likely be hidden within the large ATCA beam by the dominant emission from the quasar nucleus and/or intermediate region). New observations with higher spatial resolution and sensitivity are required both to determine the exact location of the CO in J0025A and to measure (or to set reliable limits on) the CO content of the star-forming companion nucleus.

4 DISCUSSION

4.1 SDSS J0025–10 versus local (U)LIRGs

SDSS J0025–10 is a (U)LIRG double-nuclei merging system with all observed properties consistent with those of numerous local ($z \lesssim 0.05$) LIRGs (several $\times 10^{11} \lesssim L_{\text{IR}} < 10^{12} L_{\odot}$) and ULIRGs. It shows clear morphological evidence for an ongoing major merger. That is, the double nucleus, the tidal tails, the inner spiral structure (which surrounds the QSO nucleus clockwise and apparently becomes the northern tidal tail) and the stellar clusters and/or TDGs observed along this structure (Fig. 4) are all morphological features often observed in ULIRGs and LIRGs (Monreal-Ibero et al. 2007; Haan et al. 2011; Miralles-Caballero et al. 2011). As in these systems, the star formation and probably the AGN activity are triggered by the interaction (see Alonso Herrero 2013 for a recent review; see also Bessiere et al. 2012).

³ For comparison, the SFR over the entire Milky Way is several $M_{\odot} \text{ yr}^{-1}$ (e.g. Robitaille & Whitney 2010).

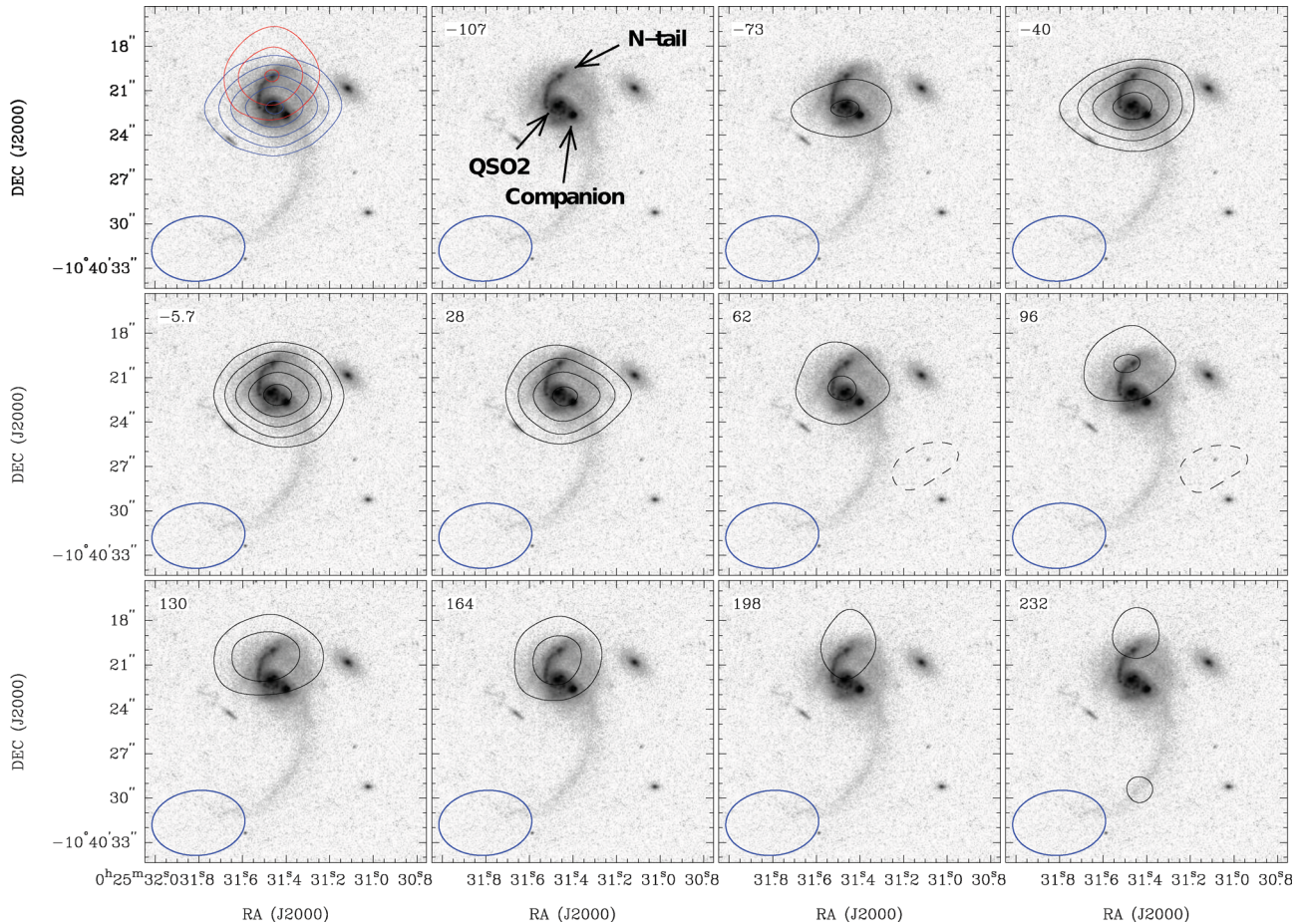


Figure 3. The total intensity image of both the blue (J0025A, $-90 \leq v \leq 79 \text{ km s}^{-1}$) and red (J0025B, $79 \leq v \leq 249 \text{ km s}^{-1}$) parts of the CO(1–0) signal is shown in the first frame, followed by the channel maps of the CO emission. Contour levels of the total intensity map are 0.27, 0.41, 0.54, 0.68 and 0.81 $\text{Jy bm}^{-1} \times \text{km s}^{-1}$. The contour level channel maps are -3.0 (dashed), 3.0, 4.5, 6.0, 7.5 and 9.0 (solid) $\times \sigma$, with $\sigma = 0.7 \text{ mJy bm}^{-1}$. The velocity values are relative to $z_{\text{sys}} = 0.3031 \pm 0.0001$. The locations of the QSO2, the companion star-forming nucleus and the northern tidal tail are indicated in the second panel. A colour version of this figure can be seen in the online version of the paper.

The IR luminosity, $L_{\text{IR}} = (1.1 \pm 0.3) \times 10^{12} L_{\odot}$, which is dominated by the starburst component, the large molecular gas content $M_{\text{H}_2} = (6 \pm 1) \times 10^9 M_{\odot}$, the SFR $= 190 \pm 52 M_{\odot} \text{ yr}^{-1}$, the star formation efficiency $\text{SFE} = L_{\text{IR}}/M_{\text{H}_2} = 183 \pm 62 L_{\odot} M_{\odot}^{-1}$ and the gas exhaustion time-scale $\tau_{\text{SF}} = M_{\text{H}_2}/\text{SFR} = 32 \pm 11 \text{ Myr}$ are all in the range of LIRGs and ULIRGs (Sanders & Mirabel 1996; Solomon & Vanden Bout 2005; Alonso Herrero 2013).

In SDSS J0025–10, one nucleus hosts the AGN, and both harbour star formation. About 20–30 per cent of local LIRGs have an optically identified AGN, with this percentage increasing with L_{IR} and becoming ~ 70 per cent for ULIRGs (e.g. Veilleux et al. 1995, 1999; Nardini et al. 2010; Yuan, Kewley & Sanders 2010). Moreover, a large fraction (~ 63 per cent) of local LIRGs and ULIRGs have double nuclei (Haan et al. 2011) with a variety of scenarios. In some cases, both nuclei host star formation and AGN activities (NGC 6240 is the most famous example; e.g. Tacconi et al. 1999; Tecza et al. 2000). In other cases, star formation is detected in both nuclei, but none seems to harbour AGN activity or to show a composite AGN + starburst spectrum, like SDSS J0025–10 (e.g. Yuan et al. 2010).

The CO gas in SDSS J0025–10 is distributed in two main spatial components, J0025A and J0025B, with masses of $(3.4 \pm 0.7) \times 10^9$ and $(2.5 \pm 0.7) \times 10^9 M_{\odot}$, respectively. These are separated by

2 arcsec or $\sim 9 \text{ kpc}$ (projected distance) in space and by 160 km s^{-1} in velocity. J0025A is preferentially associated with the quasar nucleus and/or the intermediate region between the two interacting nuclei, while J0025B is associated with the northern tidal tail. The CO(1–0) emission from the companion nucleus is not unambiguously detected, although the active star formation it hosts implies that there must be a local reservoir of $M_{\text{H}_2} \gtrsim \text{several} \times 10^8 M_{\odot}$. The CO gas in local (U)LIRGs is usually highly concentrated in the central region towards the core of the merger ($r \lesssim 1 \text{ kpc}$; e.g. Sanders & Mirabel 1996; Bryant & Scoville 1999). In addition, a significant fraction of the gas is sometimes spread over scales of 10 kpc or more. This is possibly the case of SDSS J0025–10. That is, J0025A might be the compact, central concentration (although higher spatial resolution observations are required to constrain its exact location and compactness), while J0025B might be the more extended gaseous component.

4.2 SDSS J0025–10 as a (U)LIRG–optical QSO transition object

Both theory and observations support the fact that the merger of two gas-rich progenitor galaxies forms a new, more massive elliptical galaxy (e.g. Toomre & Toomre 1972; Barnes & Hernquist 1996).

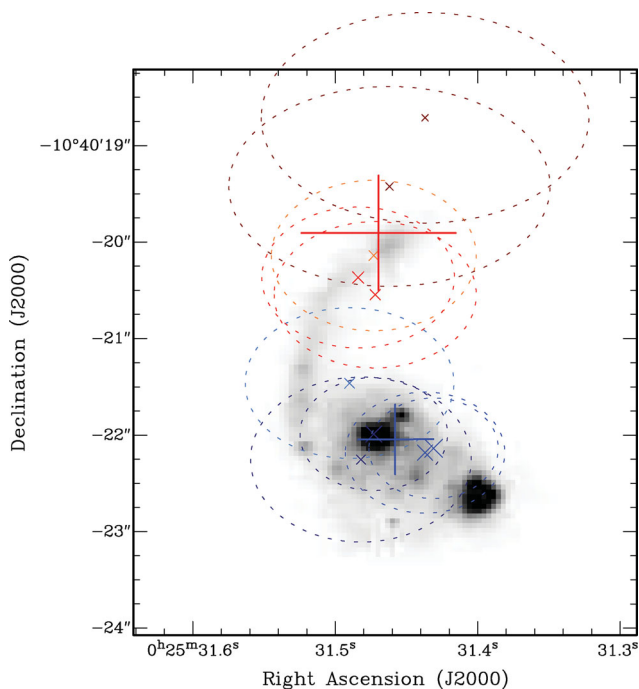


Figure 4. Overview of the location of the CO(1–0) peak emission against features seen in the *HST* image (greyscale). The large plus signs indicate the location of the peak of the CO(1–0) emission in J0025A (blue) and J0025B (red) derived from the total intensity image of Fig. 3 (see text for details). The region covered by the size of the plus symbol indicates the uncertainty in the exact location, as a result of the uncertainty in the fitting of the CO(1–0) peak combined with astrometric uncertainty (see Section 2). The crosses indicate the location of the peak of the CO(1–0) emission in the various channel maps of Fig. 3 (dark blue and dark red indicate the lowest and highest velocities, respectively). The size of the cross scales with the significance level at which CO(1–0) is detected, while the dashed ellipses indicate the uncertainty in the exact location – from the CO(1–0) fitting combined with astrometric errors. A colour version of this figure can be seen in the online version of the paper.

As a consequence of the gravitational interaction, gaseous dissipation funnels gas into the gravitational centre and triggers intense star formation, which is manifested in the (U)LIRG phenomenon. The gas inflow could also fuel the formation of an AGN (e.g. Hopkins & Beacom 2006; Hopkins, Richards & Hernquist 2008). The discovery of massive reservoirs of molecular gas shifted far away from the location of the quasar has prompted some authors to suggest that gas-poor/gas-rich galaxy mergers can also trigger quasar activity (Papadopoulos et al. 2008; Aravena et al. 2011; Riechers 2013).

We are observing SDSS J0025–10 when the galaxies are deeply interpenetrating and approaching the final coalescence ($r \lesssim$ a few kpc). Simulations of gas dynamics and starbursts in major gas-rich mergers with or without quasar activity (e.g. Mihos & Hernquist 1994; Hopkins et al. 2005) have shown that at this stage the morphologies show distorted, irregular isophotes and extended tidal tails, as observed in SDSS J0025–10. The models also predict that at this moment the gas experiences the strongest levels of inflow, so that large amounts of gas accumulate in the central region and very intense star formation activity is triggered as a consequence. The duration of the starburst is expected to be very short, ~ 50 Myr (Mihos & Hernquist 1994). The presence of such a young stellar population is confirmed in SDSS J0025–10 (see Section 1.1).

Sanders et al. (1988a) have proposed that there is a natural evolution from ULIRG to QSO. That is, ULIRGs are the ini-

tial dust-enshrouded stage of quasars, which will become optical quasars once the nuclei shed the obscuring dust via feedback mechanisms (see also Hopkins et al. 2005). Some authors have expanded the ULIRG–QSO evolutionary scenario, accommodating the LIRG phase as a phase that appears earlier in mergers than the ULIRG phase (e.g. Yuan et al. 2010; Haan et al. 2011). Recently, Rothberg et al. (2013) have provided a review of the observational and theoretical studies, including the pros and cons of these scenarios. Although the merger-driven evolutionary sequence (U)LIRG–QSO is probably too simplistic (Veilleux, Kim & Sanders 2002), both theory and observations support the fact that at least a significant fraction of optical quasars might evolve from a prior (U)LIRG phase.

In such a scenario, SDSS J0025–10 is a strong candidate to be a (U)LIRG–optical QSO transition object. All the properties investigated here are expected for such a transition phase: high IR luminosity powered by intense star formation, a rich molecular gas reservoir, strong evidence for a major merger of two gas-rich progenitors and the optical identification of quasar activity (Sanders et al. 1988a,b).

The nuclear separation in SDSS J0025–10 (~ 5 kpc) is consistent with typical values of double-nuclei LIRGs, and is significantly larger than in more advanced mergers (e.g. Yuan et al. 2010; Haan et al. 2011), which are more frequently found in ULIRGs. As well as the fact that a large fraction of the molecular gas is still unsettled, this shows that the system is in a transient stage prior to the final coalescence of the nuclei.

The identification of an ionized outflow associated with the quasar nucleus (VM11b) prompts the interesting possibility of tracing its signature in both the neutral and molecular phases in order to fully characterize its mass, geometry and energetics. This information would allow us to evaluate whether the outflow is powerful enough to clear up completely the material surrounding the quasar nucleus, to quench the star formation activity and to convert SDSS J0025–10 into an optical quasar before it becomes a non-active massive elliptical galaxy (Di Matteo, Springel & Hernquist 2005).

4.3 A large reservoir of molecular gas at the tip of the tidal tail

Merger simulations of gas-rich galaxies have shown that, besides the infalling gas that concentrates in a compact central region of less than 1 kpc in size, part of the gas survives the merger (Mihos & Hernquist 1994; Barnes & Hernquist 1996; Hopkins, Richards & Hernquist 2008). This is primarily material that has been moved to large radii temporarily, either blown out by a combination of supernova and AGN feedback or thrown out in tidal tails. The lack of spatial information prevents us from making a confident elucidation of the nature of J0025A and J0025B. However, given their spatial location, it is reasonable to propose that J0025A is (or will become) the compact component, while J0025B, which is associated with the northern tidal tail, is the surviving material.

In Fig. 4, it seems that the location of the peak of the CO(1–0) emission in the various channel maps traces the tidal tail, from the inner spiral-like structure between the nuclei to the tip of the tail, and perhaps beyond. This suggests that there is molecular gas along the tail. According to the model predictions, this surviving gas will then slowly settle back into a small, rotationally supported embedded disc (Buornaud & Duc 2006; Hopkins, Richards & Hernquist 2008) \sim a couple $\times 10^8$ yr after the coalescence. This gas is not expected to contribute much to the galaxy stellar mass (\sim a few per cent), even for the most gas-rich mergers. Thus, although a large reservoir of gas is still falling towards the centre, it seems unlikely that it will

produce a significant enhancement on the build up of the galaxy stellar mass.

The centroid of J0025B is coincident with a prominent feature that has an elliptical shape, located at the tip of the northern tidal tail and clearly identified in the *HST* image (Fig. 4). A CO accumulation at a tidal tail's tip is a promising TDG candidate (Buornd & Duc 2006). A TDG is a self-gravitating entity that consists of the debris of a galaxy interaction.

Indeed, the properties of the optical feature strongly support this scenario. The optical size along the major axis $D = 1.4 \pm 0.1$ kpc, the effective radius $R_{\text{eff}} = 0.70 \pm 0.06$ kpc, the observed $H\beta$ luminosity $L(H\beta) = 3.6 \times 10^{40}$ erg s^{-1} (VM11a) are all consistent with the values measured for TDGs (e.g. Buornd & Duc 2006; Monreal-Ibero et al. 2007). The J0025B CO(1–0) line luminosity is $\gtrsim 50$ times higher (and therefore implies $\gtrsim 50$ times more molecular gas mass) than typically measured for TDGs (e.g. Braine et al. 2001), but this most probably reflects the CO(1–0) contamination of J0025B by emission from other regions.

The dynamical mass of the TDG can be estimated as (Monreal-Ibero et al. 2007)

$$M_{\text{dyn}}(M_{\odot}) = \text{constant} \times 10^6 \frac{R_{\text{eff}}}{\text{kpc}} \left(\frac{\sigma}{\text{km s}^{-1}} \right)^2.$$

The constant value ranges between 1.4 and 2.2. Following Monreal-Ibero et al. (2007), we adopt a value of 2.09. This calculation is highly uncertain because of the uncertainty on the exact mass distribution of the object and especially on the velocity dispersion $\sigma = \text{FWHM}/2.35$. In spite of this, an estimation of the ranges allowed can be useful to support or to discard the TDG scenario. The $\text{FWHM}_{\text{CO}} = 165 \pm 85$ km s^{-1} of J0025B⁴ is not a reliable tracer of the dynamical mass, because, as we have seen, it is contaminated by emission from other regions. However, the optical emission lines, which are much less affected by this problem, have $\text{FWHM}(H\beta) \leq 140$ km s^{-1} , $\text{FWHM}([\text{O III}]\lambda 5007) = 330 \pm 10$ km s^{-1} (VM11a) and $\text{FWHM}([\text{O I}]\lambda 6300) = 140 \pm 20$ km s^{-1} . Such a discrepancy for $[\text{O III}]$ might indicate that it is broadened by some turbulent mechanism (e.g. winds). It is reasonable to assume $\text{FWHM} \sim 140$ km s^{-1} or $\sigma \sim 60$ km s^{-1} (note that this value also locates the system with other TDGs in the R_{eff} versus σ plane; e.g. Monreal-Ibero et al. 2007). In such a case, $M_{\text{dyn}} \sim 5 \times 10^9 M_{\odot}$. Dynamical masses as large as this have been measured for other TDGs (Buornd & Duc 2006; Monreal-Ibero et al. 2007). At the lowest extreme, even unexpectedly small σ values (e.g. 10 km s^{-1}) would result in $M_{\text{dyn}} > 10^8 M_{\odot}$, still typical of TDGs. Thus, in spite of the uncertainties, we confirm that the dynamical mass of the optical tidal feature associated with the J0025B centroid is in the range of a TDG.

The formation of such massive self-gravitating condensations of matter in the outer regions of tidal tails is allowed by the simulations, without strong constraints on the galactic encounter parameters (Buornd et al. 2004). These condensations can survive longer (> 1 Gyr) than the inner regions of the tails. According to these simulations, only the objects formed at the tip of tidal tails can become long-lived, massive, dwarf satellite galaxies. Whether this will be the case depends on its stability against its own internal motions and against tidal forces from the parent galaxies.

⁴ This value is larger than 80 ± 40 km s^{-1} quoted in Section 3.2 for the red fainter component of the double-horned CO profile. The reason for this is that the total CO emission associated with J0025B has been considered, rather than only the inner 2.3×2.3 arcsec² pixel used to build the one-dimensional spectrum discussed in Section 3.2.

5 SUMMARY AND CONCLUSIONS

We have characterized the amount, spatial distribution and kinematics of the molecular gas in the optically selected type 2 quasar SDSS J0025–10 at $z = 0.30$. This is a merging system with a double composite nucleus (AGN + H II). For this, we have used the CO(1–0) transition based on data obtained with the ATCA. This is one of the scarce examples of quasar host galaxies where the CO emission has been resolved spatially at any redshift.

The system contains $M_{\text{H}_2} = (6 \pm 1) \times 10^9 M_{\odot}$, which is distributed in two main reservoirs separated by ~ 9 kpc. It has been found that ~ 60 per cent of the gas is in the central region, preferentially associated with the QSO nucleus and/or the intermediate region between the two nuclei. The other 40 per cent is associated with the northern tidal tail and is therefore unsettled.

Based on WISE and *IRAS* photometry, we constrain the IR luminosity $L_{\text{IR}} = (1.1 \pm 0.3) \times 10^{12} L_{\odot}$ and show that it is dominated by a starburst, rather than the AGN. SDSS J0025–10 is an analogue of local ($z \lesssim 0.05$) LIRGs with high $L_{\text{IR}} > \text{several} \times 10^{11} L_{\odot}$ and ULIRGs. The clear morphological evidence for an ongoing major merger, the large molecular gas content, the star formation rate $\text{SFR} = 190 \pm 52 L_{\odot} M_{\odot}^{-1}$, the star formation efficiency $\text{SFE} = 183 \pm 62 L_{\odot} M_{\odot}^{-1}$ and the gas exhaustion time-scale $\tau_{\text{SF}} = 32 \pm 11$ Myr are all in the range of these local systems.

SDSS J0025–10 is the result of an ongoing major merger of two gas-rich progenitors. Together with the high IR luminosity dominated by a starburst, the massive reservoir of molecular gas and the quasar activity, this is consistent with a transition phase in the (U)LIRG–optical QSO evolutionary scenario. Moreover, the relatively large nuclear separation (~ 5 kpc) and the existence of large amounts of unsettled molecular gas (probably surviving gas from the merger) suggest that we are observing the system during a particular transient phase, prior to more advanced mergers where the nuclei have already coalesced.

We propose that at least part of the extended, unsettled reservoir of molecular gas is associated with a TDG at the tip of the northern tidal tail identified in the *HST* image. The formation of TDGs in the outer regions of tidal tails is predicted by simulations of colliding galaxies.

ACKNOWLEDGEMENTS

The authors wish to thank an anonymous referee for useful comments that have helped to improve the paper substantially. They also thank Luis Colina for useful discussions and suggestions for the manuscript.

This work has been funded with support from the Spanish former Ministerio de Ciencia e Innovación through the grant AYA2010-15081. MR acknowledges support by the Spanish MINECO through grant AYA 2012-38491-C02-02, co-funded with FEDER funds. ATCA is funded by the Commonwealth of Australia for operation as a National Facility managed by the Commonwealth Scientific and Industrial Research Organization (CSIRO).

REFERENCES

- Alonso Herrero A., 2013, Proceedings of Science, preprint (arXiv:1302.2033)
- Aravena M., Wagg J., Papadopoulos P., Feain I., 2011, *ApJ*, 737, 64
- Barnes J. E., Hernquist L., 1996, *ApJ*, 471, 115
- Bertram T., Eckart A., Fischer S., Zuther J., Straubmeier C., Wisotzki L., Krips M., 2007, *A&A*, 470, 571

- Bessiere P., Tadhunter C., Ramos Almeida C., Villar Martín M., 2012, *MNRAS*, 426, 276
- Bournaud F., Duc P. A., 2006, *A&A*, 456, 481
- Bournaud F., Duc P. A., Amram P., Combes F., Gach J. L., 2004, *A&A*, 425, 813
- Braine J., Duc P., Linsfeld U., Charmandaris V., Vallejo O., Leon S., Brinks E., 2001, *A&A*, 378, 51
- Briggs D. S., 1995, PhD thesis, New Mexico Tech
- Bryant P. M., Scoville N. Z., 1999, *AJ*, 117, 2632
- Carilli C. et al., 2002, *ApJ*, 575, 145
- Carilli C. et al., 2010, *ApJ*, 714, 1407
- Di Matteo T., Springel V., Hernquist L., 2005, *Nat*, 433, 605
- Downes D., Solomon P., 1998, *ApJ*, 507, 615
- Emonts B. et al., 2011, *MNRAS*, 415, 655
- Feruglio C., Maiolino R., Piconcelli E., Menci N., Aussel H., Lamastra A., Fiore F., 2010, *A&A*, 518, L155
- Haan S. et al., 2011, *AJ*, 141, 100
- Hopkins P., Beacom J., 2006, *ApJ*, 651, 142
- Hopkins P. F., Hernquist L., Martini P., Cox T. J., Robertson B., Di Matteo T., Springel V., 2005, *ApJ*, 625, L71
- Hopkins P., Hernquist L., Cox T., Dutta S. N., Rothberg B., 2008, *ApJ*, 679, 156
- Kennicutt R., 1998, *ARA&A*, 36, 189
- Krips M., Eckart A., Neri R., Bertram T., Straubmeier C., Fischer S., Staguhn J. G., Vogel S. N., 2007, *A&A*, 464, 187
- Krips M., Neri R., Cox P., 2012, *ApJ*, 753, 135
- Martínez Sansigre A. et al., 2009, *ApJ*, 706, 184
- Middelberg E., Sault R., Kesteven M., 2006, *PASA*, 23, 147
- Mihos J. C., Hernquist L., 1994, *ApJ*, 431, L9
- Miralles-Caballero D., Colina L., Arribas S., Duc P. A., 2011, *AJ*, 142, 79
- Monreal-Ibero A., Colina L., Arribas S., García-Marín M., 2007, *A&A*, 472, 421
- Nardini E., Risaliti G., Watabe Y., Salvati M., Sani E., 2010, *MNRAS*, 405, 2505
- Norris R. P., Mao M. Y., Lenc E., Emonts B., Sharp R. G., 2013, in *Mangum J. G., ed., NRAO Conf. Ser. Vol. 28, The Interstellar Medium in High Redshift Galaxies Comes of Age*. NRAO, Charlottesville, VA
- Papadopoulos P., Ivison R., Carilli C., Lewis G., 2001, *Nat*, 409, 58
- Papadopoulos P., Feain I., Wagg J., Wilner D., 2008, *ApJ*, 684, 845
- Polletta M., Weedman D., Hönig S., Lonsdale C., Smith H., Houck J., 2008, *ApJ*, 675, 960
- Ramos Almeida C. et al., 2012, *MNRAS*, 419, 687
- Riechers D., 2013, *ApJ*, 765, L31
- Robitaille P., Whitney B., 2010, *ApJ*, 710, 11
- Rodríguez-Zaurín J., Arribas S., Monreal-Ibero A., Colina L., Alonso-Herrero A., Alfonso-Garzón J., 2011, *A&A*, 527, 60
- Rothberg B., Fischer J., Rodrigues M., Sanders D. B., 2013, *ApJ*, 767, 72
- Sanders D. B., Mirabel F., 1996, *ARA&A*, 34, 749
- Sanders D. B., Soifer T. B., Elias J. H., Madore B. F., Matthews K., Neugebauer G., 1988a, *ApJ*, 325, 74
- Sanders D. B., Soifer T. B., Elias J. H., Neugebauer G., Matthews K., 1988b, *ApJ*, 328, L35
- Sault R., Teuben P., Wright M., 1995, in *Shaw R. A., Payne H. E., Hayes J. J. E., eds, ASP Conf. Ser. Vol. 77, Astronomical Data Analysis Software and Systems IV*. Astron. Soc. Pac., San Francisco, p. 433
- Solomon P., Vanden Bout P., 2005, *ARA&A*, 43, 677
- Staguhn J., Schinnerer E., Eckart A., Scharwächter J., 2004, *ApJ*, 609, 85
- Tacconi L., Genzel R., Tezcla M., Gallimore J. F., Downes D., Scoville Z., 1999, *AJ*, 524, 732
- Tadhunter C. et al., 2011, *MNRAS*, 412, 960
- Tecza M., Genzel R., Tacconi L., Anders S., Tacconi-Garman L., Thatte N., 2000, *ApJ*, 537, 178
- Toomre A., Toomre J., 1977, *ApJ*, 178, 623
- Veilleux S., Kim D. C., Sanders D. B., Mazzarella J. M., Soifer B. T., 1995, *ApJS*, 98, 171
- Veilleux S., Kim D. C., Sanders D. B., 1999, *ApJ*, 522, 113
- Veilleux S., Kim D. C., Sanders D. B., 2002, *ApJS*, 143, 315
- Vernet J., Fosbury R. A. E., Villar-Martín M., Cohen M. H., Cimatti A., di Serego Alighieri S., Goodrich R. W., 2001, *A&A*, 366, 7
- Villar-Martín M., Tadhunter C., Humphrey A., Fraga Encina R., González Delgado R., Pérez Torres M., Martínez-Sansigre A., 2011a, *MNRAS*, 416, 262 (VM11a)
- Villar-Martín M., Humphrey A., González Delgado R., Colina L., Arribas S., 2011b, *MNRAS*, 418, 2032 (VM11b)
- Villar-Martín M., Cabrera Lavers A., Bessiere P., Tadhunter C., Rose M., de Breuck C., 2012, *MNRAS*, 423, 80
- Villar-Martín M., Rodríguez M., Drouart G. et al., 2013, *MNRAS*, submitted
- Westmoquette M. S., Clements D. L., Bendo G. J., Khan S. A., 2012, *MNRAS*, 424, 416
- Xia X. Y. et al., 2012, *ApJ*, 750, 92
- Yuan T. T., Kewley L. S., Sanders D. B., 2010, *ApJ*, 709, 884
- Zakamska N. et al., 2003, *AJ*, 126, 2125

This paper has been typeset from a $\text{\TeX}/\text{\LaTeX}$ file prepared by the author.